Available online at www.sciencedirect.com
SCIENCE DIRECT®
Journal of Computational Physics 189 (2003) 557–578
JOURNAL OF COMPUTATIONAL PHYSICS
www.elsevier.com/locate/jcp

A free-surface correction method for simulating shallow water flows

XinJian Chen *

Surface Water Improvement and Management Program, Southwest Florida Water Management District, 7601 Highway 301 North Tampa, FL 33637, USA

Received 17 October 2002; received in revised form 14 April 2003; accepted 17 April 2003

Abstract

This paper presents a free-surface correction (FSC) method for solving the 3-D shallow water equations. Under the hydrostatic pressure assumption, the FSC method solves the governing equations for shallow water flows in two steps. First, an intermediate free surface is obtained after the horizontal momentum equations are solved with the explicit discretization of the pressure gradient terms. In the second step, the intermediate free surface is corrected by solving a five-diagonal matrix system for the free-surface change ($\Delta\eta$) over the time step Δt. The final velocity field is then corrected once the final free surface is obtained. The numerical scheme involves a semi-implicit discretization of the barotropic terms in the momentum equations and the horizontal fluxes terms in the vertically integrated continuity equation. Optinally, the FSC method is reduced to an explicit method for gravity waves, with the correction step omitted. Using the FSC method, a semi-implicit, 3-D finite difference model for free-surface flows has been developed. The model is mass conservative both locally and globally and is unconditionally stable with respect to gravity waves, wind and bottom stresses, and vertical eddy viscosity terms. Because both steps are straightforward and can be easily carried out, the FSC method presented here is an efficient method for simulating shallow water flows.
© 2003 Elsevier Science B.V. All rights reserved.

Keywords: Free-surface flows; Shallow water flows; Free-surface correction method; Finite difference method; Five-diagonal matrix; Bi-CGSTAB; Mass conservation

1. Introduction

Sophisticated hydrodynamic models have been widely used for design, diagnostic, or predictive purposes when dealing with complicated flow problems in a water body. For shallow water flows in lakes and estuaries, the hydrostatic pressure assumption is generally valid in most cases. Situations where the hydrostatic pressure assumption may be questionable are discussed in several previous publications [8,10,23,24].

* Tel.: 1-813-985-7481; fax: 1-813-987-6747.
E-mail address: xinjian.chen@swfwmd.state.fl.us (X. Chen).

0021-9991/$ - see front matter © 2003 Elsevier Science B.V. All rights reserved.
doi:10.1016/S0021-9991(03)00234-1

With the hydrostatic assumption and the use of the Boussinesq approximation, governing equations for free surface flows in shallow lakes and estuaries have the following forms:

$$\frac{\partial u}{\partial x}+\frac{\partial v}{\partial y}+\frac{\partial w}{\partial z}=0, \tag{1}$$

$$\frac{\partial u}{\partial t}+\frac{\partial uu}{\partial x}+\frac{\partial vu}{\partial y}+\frac{\partial wu}{\partial z}=fv-\frac{1}{\rho_0}\frac{\partial p}{\partial x}+\frac{\partial}{\partial x}\left(A_{\mathrm{h}}\frac{\partial u}{\partial x}\right)+\frac{\partial}{\partial y}\left(A_{\mathrm{h}}\frac{\partial u}{\partial y}\right)+\frac{\partial}{\partial z}\left(A_{\mathrm{v}}\frac{\partial u}{\partial z}\right), \tag{2}$$

$$\frac{\partial v}{\partial t}+\frac{\partial uv}{\partial x}+\frac{\partial vv}{\partial y}+\frac{\partial wv}{\partial z}=-fu-\frac{1}{\rho_0}\frac{\partial p}{\partial y}+\frac{\partial}{\partial x}\left(A_{\mathrm{h}}\frac{\partial v}{\partial x}\right)+\frac{\partial}{\partial y}\left(A_{\mathrm{h}}\frac{\partial v}{\partial y}\right)+\frac{\partial}{\partial z}\left(A_{\mathrm{v}}\frac{\partial v}{\partial z}\right), \tag{3}$$

$$p=g\int_z^{\eta}\rho\,\mathrm{d}\zeta, \tag{4}$$

where ρ_0 is the reference density; x, y, and z are Cartesian coordinates (x is from west to east, y is from south to north, and z is vertical pointing upward); u, v, and w are velocities in the x-, y-, and, z-directions, respectively; t, f, g, ρ, η, and p denote time, the Coriolis parameter, the gravitational acceleration, density, the free surface elevation, and pressure, respectively; and A_{h} and A_{v} represent horizontal and vertical eddy viscosities, respectively.

Eq. (1) is the continuity equation and can be integrated over the water depth to get an equation for the free surface

$$\frac{\partial \eta}{\partial t}+\frac{\partial}{\partial x}\left(\int_{h_0}^{\eta}u\,\mathrm{d}z\right)+\frac{\partial}{\partial y}\left(\int_{h_0}^{\eta}v\,\mathrm{d}z\right)=r, \tag{5}$$

where h_0 is the bottom elevation and r is the net rain intensity (precipitation minus evaporation) in cm/s. The above equation is obtained with the assumption that the flux through the bed is zero.

Free surface flows in shallow lakes and estuaries contain both fast propagating surface gravity waves and slow moving internal gravity waves. Most existing 3-D models for free surface flows solve Eqs. (1)–(5) utilizing a mode-splitting technique [1–5] in which the vertically integrated equations (external mode) are separated from the 3-D momentum equations (internal mode). The external mode solves vertically integrated equations explicitly with a small time step dictated by the Courant–Friedrichs–Levy (CFL) condition for the fast propagating gravity waves. According to this condition, stable solutions can only be obtained when the ratio of horizontal spacing (Δx) over the time step (Δt) is not larger than the celerity of the gravity wave if an explicit finite difference scheme is used. A grid Courant number (Cr) for gravity waves can be defined as $Cr = c\Delta t/\Delta x$, where c is the celerity of the gravity wave ($c=\sqrt{gD}$ for shallow waters, where D is the water depth). The CFL condition for gravity waves is equivalent to $Cr \leqslant 1$. For the internal mode, a much larger time step is allowed because effects of fast propagating external mode have been removed. The principal advantage of the mode-splitting technique is some savings in computing time, because the vertically integrated, barotropic equations governing external modes are much simpler to solve. The vertical structures of flows, on the other hand, are more expensive to solve and can be computed at much larger time steps due to the slow propagation of internal gravity waves. The challenge of this method is to ensure that the two calculations are consistent and synchronous with each other at each internal time step, which is not necessarily guaranteed.

Recent developments in 3-D hydrodynamic models involved the use of a semi-implicit method [6], which does not require the splitting of the external and internal modes. Following the similar procedure used by

Casulli [7] for 2-D shallow water flows, the semi-implicit method used in Casulli and Cheng [6] discretizes the barotropic pressure gradient terms in the horizontal momentum equations and the vertically integrated continuity equation implicitly. At each time step, the free surface is first calculated by solving a five diagonal system for η, followed by the calculation of the velocity field. According to Casulli and Cheng [6], Casulli and Stelling [8], and Casulli [9], this semi-implicit method is very efficient, because it allows the use of a large time step, which does not depend on the fast propagating surface gravity wave.

This paper presents a free-surface correction (FSC) method that, similar to the semi-implicit method of Casulli and Cheng [6], does not involve the mode-splitting procedure either, yet allows a very large time step to be used in model runs. In this method, direct solutions to Eqs. (1)–(5) are carried out with two steps. In the first step, an intermediate velocity field is solved using the free surface of the previous time step. An intermediate free surface is then calculated from Eq. (5) using the intermediate velocity field. In the second step, the intermediate free surface is corrected by solving a five-diagonal system, followed by a correction to the intermediate velocity field. The FSC method is implemented in a Lake and Estuarine Simulation System in Three Dimensions (LESS3D), a coupled simulation system of hydrodynamics, sediment transport processes, and nutrient dynamics for lakes and estuaries. Besides the flow field, the hydrodynamic portion of the model also solves salinity and temperature equations. Although the hydrostatic pressure assumption is used in the following sections for the presentation of the FSC method, the model has a non-hydrostatic module that allows fully hydrodynamic simulations of 3-D flows [10,23].

2. A FSC method for 3-D flows

The finite difference method is used to solve Eqs. (1)–(5) in a Cartesian grid system with a staggered grid arrangement of model variables. Fig. 1 shows the horizontal and vertical views of the computational stencil

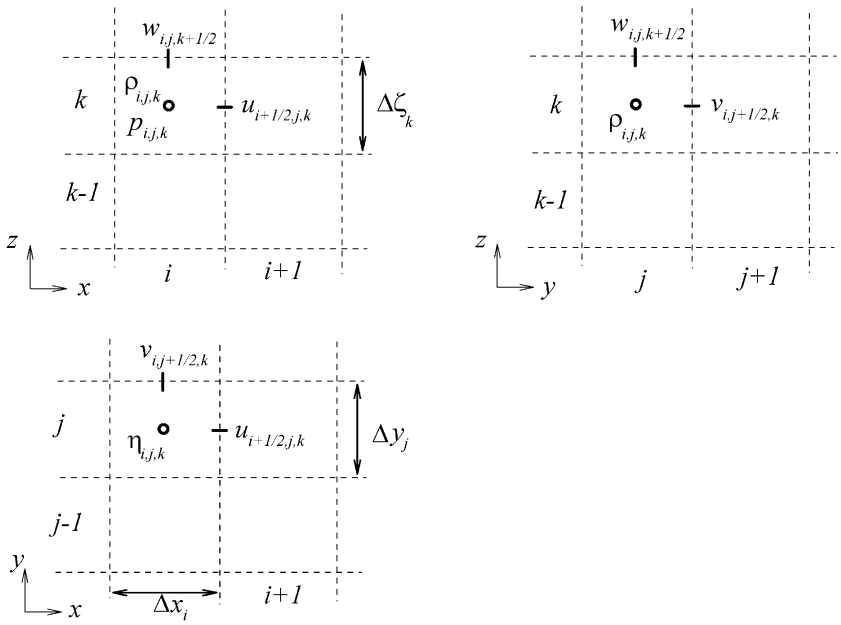

Fig. 1. A Cartesian grid system used in the LESS3D model with a staggered arrangement of model variables. The top-left graph is a view looking north, while the top-right and bottom graphs are views looking west and downward, respectively.

in Cartesian coordinates. In Fig. 1, Δx, Δy, and $\Delta\zeta$ are grid spacings in x-, y-, and z-directions, respectively. Lower case letters i, j, and k are grid indexes in the three directions. While Δx varies only with i, Δy varies only with j. $\Delta\zeta$ denotes the thickness of the horizontal layer, which is constant for the same k-index. To fit the bottom topography and the free surface, Δz for the actual cell height is used in the computation. Except for the bottom and top layers, Δz is the same as $\Delta\zeta$, the layer thickness. For the bottom layer, Δz is the distance between the top of the bottom layer and the real bottom. Similarly, for the top layer, Δz is the distance between the free surface and the bottom of the top layer. As a result, Δz is generally not the same as $\Delta\zeta$ for both the bottom and top layers. To ensure the vertical resolution near the free surface, the k-index for the top layer is allowed to vary with horizontal location and time. This eliminates the use of a thick top layer to cover the free-surface variation and allows the surface to travel from one layer to another. At each time step, the k-index for the top layer (k_m) is calculated and saved. If the free surface at the $n+1$th time step drops below the middle point of the top layer, the top cell is aggregated to the cell below it and k_m is reduced by 1. On the other hand, if the free surface at the new time step is higher than the middle point of Layer k_m+1, the top cell at the previous time step is split into two cells and the top one is the new top cell at the new time step.

With a staggered arrangement of model variables, u and v are defined at the centers of the east and north faces of the cell, respectively, while w is defined at the center of the top face. ρ, p, and concentrations are defined at the center of the cell. The surface elevation (η) and water depth (D) are defined at the center of the horizontal grid.

Substituting p in Eq. (4) into Eqs. (2) and (3) and using the Leibnitz integration law and the Boussinesq approximation, Eqs. (2) and (3) can be written as

$$\frac{\partial u}{\partial t} = fv - g\frac{\partial \eta}{\partial x} - \frac{g}{\rho_0}\int_z^{\eta}\frac{\partial \rho}{\partial x}\,\mathrm{d}\zeta + \frac{\partial}{\partial z}\left(A_{\mathrm{v}}\frac{\partial u}{\partial z}\right) + H_x, \tag{6}$$

$$\frac{\partial v}{\partial t} = -fu - g\frac{\partial \eta}{\partial y} - \frac{g}{\rho_0}\int_z^{\eta}\frac{\partial \rho}{\partial y}\,\mathrm{d}\zeta + \frac{\partial}{\partial z}\left(A_{\mathrm{v}}\frac{\partial v}{\partial z}\right) + H_y, \tag{7}$$

where H_x and H_y include the convective terms and horizontal eddy viscosity terms

$$H_x = -\frac{\partial uu}{\partial x} - \frac{\partial vu}{\partial y} - \frac{\partial wu}{\partial z} + \frac{\partial}{\partial x}\left(A_{\mathrm{h}}\frac{\partial u}{\partial x}\right) + \frac{\partial}{\partial y}\left(A_{\mathrm{h}}\frac{\partial u}{\partial y}\right), \tag{8}$$

$$H_y = -\frac{\partial uv}{\partial x} - \frac{\partial vv}{\partial y} - \frac{\partial wv}{\partial z} + \frac{\partial}{\partial x}\left(A_{\mathrm{h}}\frac{\partial v}{\partial x}\right) + \frac{\partial}{\partial y}\left(A_{\mathrm{h}}\frac{\partial v}{\partial y}\right). \tag{9}$$

Density in above equations is a function of temperature and salinity [26]. The governing continuity equations for mass (1) and momentum (6) and (7) are supplemented with the following advection–diffusion equation for concentrations:

$$\frac{\partial \Phi}{\partial t} + \frac{\partial u\Phi}{\partial x} + \frac{\partial v\Phi}{\partial y} + \frac{\partial w\Phi}{\partial z} = \frac{\partial}{\partial x}\left(B_{\mathrm{h}}\frac{\partial \Phi}{\partial x}\right) + \frac{\partial}{\partial y}\left(B_{\mathrm{h}}\frac{\partial \Phi}{\partial y}\right) + \frac{\partial}{\partial z}\left(B_{\mathrm{v}}\frac{\partial \Phi}{\partial z}\right) + S_{\mathrm{s}}, \tag{10}$$

where S_{s} represents the sink/source terms; Φ can be temperature, salinity, suspended sediment concentrations, or nutrient concentrations; and B_{h} and B_{v} are eddy diffusivities in the horizontal and vertical directions, respectively. In the above transport equation, if the material simulated involves settling, w in the advective term includes the settling velocity of the material.

In the first step of the FSC method, an intermediate velocity field is first calculated from Eqs. (6) and (7) using the pressure field of the previous time step

$$\frac{u^{n+*}-u^n}{\Delta t}=fv^n-g\frac{\partial\eta^n}{\partial x}-\frac{g}{\rho_0}\left[\int_z^\eta\frac{\partial\rho}{\partial x}\,\mathrm{d}\zeta\right]^n+H_x^n+\frac{\partial}{\partial z}\left(A_\mathrm{v}\frac{\partial u^{n+*}}{\partial z}\right), \tag{11}$$

$$\frac{v^{n+*}-v^n}{\Delta t}=-fu^{n+*}-g\frac{\partial\eta^n}{\partial y}-\frac{g}{\rho_0}\left[\int_z^\eta\frac{\partial\rho}{\partial y}\,\mathrm{d}\zeta\right]^n+H_y^n+\frac{\partial}{\partial z}\left(A_\mathrm{v}\frac{\partial v^{n+*}}{\partial z}\right) \tag{12}$$

where Δt is the time step used in the computation, the superscript n represents the previous time step, while the superscript $n+*$ represents intermediate solutions at the new time step. For simplicity, the i-, j-, and k-indexes are omitted in the above finite difference equations.

In Eqs. (11) and (12), the vertical eddy viscosity terms are discretized implicitly, while the horizontal gradients of the free surface, H_x, and H_y, and the baroclinic terms are treated explicitly. For the Coriolis terms, the newest available velocity component is always used in the computation. For example, when u^{n+*} is first calculated from Eq. (11), v^n is used; however, when v^{n+*} is calculated from Eq. (12), u^{n+*} is used. To avoid that the calculation of v^{n+*} always uses a newer u-velocity, Eqs. (11) and (12) are solved in an alternate sequence in the computations: First Eq. (11) and then Eq. (12) at the odd time step, but reverse the sequence at the even time step. When Eq. (12) is solved first, u^n is used in the Coriolis term of the v-equation, but the newly available intermediate v-velocity (v^{n+*}) is used in the Coriolis term for the calculation of u^{n+*}.

Boundary conditions in the horizontal directions are specified with either free surface elevations or velocities for open boundaries. At solid boundary, normal velocity is set to zero, thereby implying appropriate Neumann-type boundary conditions for pressure. Boundary conditions at the free surface and at the bottom are implicitly specified by wind and bottom shear stresses, respectively:

$$\left[A_\mathrm{v}\frac{\partial u^{n+*}}{\partial z}\right]_{z=\eta}=\frac{\tau_{\eta x}}{\rho_\eta},\quad \left[A_\mathrm{v}\frac{\partial v^{n+*}}{\partial z}\right]_{z=\eta}=\frac{\tau_{\eta y}}{\rho_\eta}, \tag{13}$$

$$\left[A_\mathrm{v}\frac{\partial u^{n+*}}{\partial z}\right]_{z=h_0}=C_\mathrm{d}\rho u_\mathrm{b}^{n+*}\sqrt{u_\mathrm{b}^{n^2}+v_\mathrm{b}^{n^2}},\quad \left[A_\mathrm{v}\frac{\partial v^{n+*}}{\partial z}\right]_{z=h_0}=C_\mathrm{d}\rho v_\mathrm{b}^{n+*}\sqrt{u_\mathrm{b}^{n^2}+v_\mathrm{b}^{n^2}}, \tag{14}$$

where $\tau_{\eta x}$ and $\tau_{\eta y}$ denote wind shear stresses in x- and y-directions, respectively; u_b and v_b are velocities of the bottom cell in x- and y-directions, respectively; and C_d is the bottom frictional coefficient which can be estimated by assuming a log-layer distribution of velocity for fully developed turbulence

$$C_\mathrm{d}=\left[\frac{\kappa}{\ln(z_\mathrm{b}/z_0)}\right]^2, \tag{15}$$

where κ is the von Karman constant (0.41), z_b is the z-coordinate of the center of the bottom cell, $z_0=k_\mathrm{s}/30$ and k_s is the bottom roughness. Note that external fluxes at the bottom and at the free surface are included in the calculation of the free-surface location using Eq. (5).

Because of the explicit treatment of the horizontal gradients of the free surface in the calculations of the intermediate velocities, Eqs. (11) and (12) are two tri-diagonal matrix systems and can be efficiently solved using the Thomas Algorithm. It is easy to generate the tri-diagonal matrix systems from Eqs. (11) and (12) because only the vertical eddy viscosity terms and the bottom shear stresses are implicit. Once u^{n+*} and v^{n+*} are solved, the intermediate vertical velocity and the intermediate free surface can be computed using Eqs. (1) and (5), respectively, with the following finite difference forms:

$$w_{i,j,k}^{n+*}=\frac{1}{a_{i,j,k+1/2}^n}[F_{i,j,k-1/2}^{n+*}-F_{i+1/2,j,k}^{n+*}+F_{i-1/2,j,k}^{n+*}-F_{i,j+1/2,k}^{n+*}+F_{i,j-1/2,k}^{n+*}], \tag{16}$$

$$\Delta\eta^*_{i,j} = \eta^{n+*}_{i,j} - \eta^n_{i,j} = -\frac{\Delta t(1-\theta)}{a^\tau_{i,j}}[U^n_{i+1/2,j} - U^n_{i-1/2,j} + V^n_{i,j+1/2} - V^n_{i,j-1/2}] - \frac{\Delta t\theta}{a^\tau_{i,j}}[U^{n+*}_{i+1/2,j} - U^{n+*}_{i-1/2,j} + V^{n+*}_{i,j+1/2} - V^{n+*}_{i,j-1/2}] + \Delta t r^{n+1/2}, \tag{17}$$

where $a^n_{i,j,k+1/2}$ is the area of the top face of the cell with the indexes i, j, and k at the previous time step, $a^\tau_{i,j}$ is the wet surface area of the horizontal grid with the indexes i and j at the previous time step, $F^{n+*}_{i-1/2,j,k}$, $F^{n+*}_{i,j-1/2,k}$ and $F^{n+*}_{i,j,k-1/2}$ are fluxes of water flowing into cell (i, j, k) through the west, south, and bottom faces, respectively, $\Delta\eta^*_{i,j}$ $(= \eta^{n+*}_{i,j} - \eta^n_{i,j})$ is the increment of the free surface estimated from the intermediate velocity field, or the difference between the intermediate free surface and the free surface at the previous time step, θ is an implicitness parameter varying between 0 and 1, and U and V are vertically integrated fluxes:

$$\begin{aligned} U^n_{i+1/2,j} &= \sum_{k=k_{un}}^{k_{um}} u^n_{i+1/2,j,k} a^n_{i+1/2,j,k}, \quad V^n_{i,j+1/2} = \sum_{k=k_{vn}}^{k_{vm}} v^n_{i,j+1/2,k} a^n_{i,j+1/2,k}, \\ U^{n+*}_{i+1/2,j} &= \sum_{k=k_{un}}^{k_{um}} u^{n+*}_{i+1/2,j,k} a^n_{i+1/2,j,k}, \quad V^{n+*}_{i,j+1/2} = \sum_{k=k_{vn}}^{k_{vm}} v^{n+*}_{i,j+1/2,k} a^n_{i,j+1/2,k}, \end{aligned} \tag{18}$$

where $a^n_{i+1/2,j,k}$ and $a^n_{i,j+1/2,k}$ are areas of the east and north faces, respectively, of the cell with the indexes i, j, and k at the previous time step, k_{un} and k_{um} are, respectively, the bottom and top k-indexes at the u-point, and k_{vn} and k_{vm} are the bottom and top k-indexes at the v-point.

If we change the superscript $n+*$ to $n+1$, then the computation continues to the next time step (time step $n+2$). However, the time step (Δt) will be restricted by the celerity of the gravity wave due to the explicit treatment of the free-surface gradient terms in the momentum equations. This is not desirable. To eliminate this time step restriction caused by the explicit treatment of the barotropic terms, the second step of the FSC method is introduced.

Let us change the horizontal gradients of the free surface in Eqs. (11) and (12) from explicit to semi-implicit and change the superscript $n+*$ to $n+1$ except for the Coriolis term. We have:

$$\frac{u^{n+1}-u^n}{\Delta t} = fv^n - g(1-\theta)\frac{\partial\eta^n}{\partial x} - g\theta\frac{\partial\eta^{n+1}}{\partial x} - \frac{g}{\rho_0}\left[\int_z^\eta \frac{\partial\rho}{\partial x}\,\mathrm{d}\zeta\right]^n + H^n_x + \frac{\partial}{\partial z}\left(A_\mathrm{v}\frac{\partial u^{n+1}}{\partial z}\right), \tag{19}$$

$$\frac{v^{n+1}-v^n}{\Delta t} = -fu^{n+*} - g(1-\theta)\frac{\partial\eta^n}{\partial y} - g\theta\frac{\partial\eta^{n+1}}{\partial y} - \frac{g}{\rho_0}\left[\int_z^\eta \frac{\partial\rho}{\partial y}\,\mathrm{d}\zeta\right]^n + H^n_y + \frac{\partial}{\partial z}\left(A_\mathrm{v}\frac{\partial v^{n+1}}{\partial z}\right), \tag{20}$$

where u^{n+1} and v^{n+1} are final velocities at the new time step.

Subtracting Eqs. (11) and (12) from Eqs. (19) and (20), respectively, we have:

$$\frac{\delta u}{\Delta t} = -g\theta\frac{\partial(\Delta\eta)}{\partial x} + \frac{\partial}{\partial z}\left[A_\mathrm{v}\frac{\partial(\delta u)}{\partial z}\right], \tag{21}$$

$$\frac{\delta v}{\Delta t} = -g\theta\frac{\partial(\Delta\eta)}{\partial y} + \frac{\partial}{\partial z}\left[A_\mathrm{v}\frac{(\delta v)}{\partial z}\right], \tag{22}$$

where $\Delta\eta(= \eta^{n+1} - \eta^n)$ is the final increment of the free surface over the time step Δt, $\delta u = u^{n+1} - u^{n+*}$ and $\delta v = v^{n+1} - v^{n+*}$. Therefore, Eqs. (21) and (22) are equations for velocity corrections δu and δv. Integrating both equations over the water column, we have:

$$U^{n+1}_{i+1/2,j} = U^{n+*}_{i+1/2,j} - g\Delta t\theta \frac{\partial(\eta^{n+1} - \eta^n)}{\partial x} A^n_{i+1/2,j}, \tag{23}$$

$$V^{n+1}_{i,j+1/2} = V^{n+*}_{i,j+1/2} - g\Delta t\theta \frac{\partial(\eta^{n+1} - \eta^n)}{\partial y} A^n_{i,j+1/2}, \tag{24}$$

where $A^n_{i+1,j}$ and $A^n_{i,j+1/2}$ are total areas of the east and north faces of the water column for a horizontal grid with the indexes i and j at the nth time step. Note that the same boundary conditions specified in Eqs. (13) and (14) have been used for the final velocity field, therefore:

$$\left[A_{\mathrm{v}} \frac{\partial(\delta u)}{\partial z}\right]_{z=\eta} = \left[A_{\mathrm{v}} \frac{\partial(\delta u)}{\partial z}\right]_{z=h_0} = 0, \tag{25}$$

$$\left[A_{\mathrm{v}} \frac{\partial(\delta v)}{\partial z}\right]_{z=\eta} = \left[A_{\mathrm{v}} \frac{\partial(\delta v)}{\partial z}\right]_{z=h_0} = 0. \tag{26}$$

The final free-surface increment over the time step (Δt) is found from the following discrete form of Eq. (5):

$$\begin{aligned}\Delta\eta_{i,j} = \eta^{n+1}_{i,j} - \eta^n_{i,j} = &-\frac{\Delta t(1-\theta)}{a^\tau_{i,j}}[U^n_{i+1/2,j} - U^n_{i-1/2,j} + V^n_{i,j+1/2} - V^n_{i,j-1/2}] \\ &-\frac{\Delta t\theta}{a^\tau_{i,j}}[U^{n+1}_{i+1/2,j} - U^{n+1}_{i-1/2,j} + V^{n+1}_{i,j+1/2} - V^{n+1}_{i,j-1/2}] + \Delta t r^{n+1/2}.\end{aligned} \tag{27}$$

Note that the above equation is similar to Eq. (17). Inserting Eqs. (23) and (24) into Eq. (27) and then combining with Eq. (17), one obtains

$$\begin{aligned}\eta^{n+1}_{i,j} - \eta^{n+*}_{i,j} = \frac{g\Delta t^2\theta^2}{a^\tau_{i,j}} \Bigg[&A^n_{i+1/2,j}\frac{\Delta\eta_{i+1,j} - \Delta\eta_{i,j}}{\Delta x_{i+1/2}} - A^n_{i-1/2,j}\frac{\Delta\eta_{i,j} - \Delta\eta_{i-1,j}}{\Delta x_{i-1/2}} + A^n_{i,,j+1/2}\frac{\Delta\eta_{i,j+1} - \Delta\eta_{i,j}}{\Delta y_{j+1/2}} \\ &- A^n_{i,j-1/2}\frac{\Delta\eta_{i,j} - \Delta\eta_{i,j-1}}{\Delta y_{j-1/2}}\Bigg].\end{aligned} \tag{28}$$

Eq. (28) can be seen as an equation for the correction of the free surface because its right-hand side is the difference between the final and intermediate free surfaces. This is the source of the name free-surface correction (FSC) method. Eq. (28) can be rewritten in the following form:

$$-R^s_{i,j}\Delta\eta_{i,j-1} - R^w_{i,j}\Delta\eta_{i-1,j} + (1 + R^s_{i,j} + R^w_{i,j} + R^e_{i,j} + R^n_{i,j})\Delta\eta_{i,j} - R^e_{i,j}\Delta\eta_{i+1,j} - R^n_{i,j}\Delta\eta_{i,j+1} = \Delta\eta^*_{i,j}, \tag{29}$$

where

$$\begin{aligned}R^w_{i,j} &= \frac{g\Delta t^2\theta^2}{a^\tau_{i,j}\Delta x_{i-1/2}} A_{i-1/2,j}, \quad R^e_{i,j} = \frac{g\Delta t^2\theta^2}{a^\tau_{i,j}\Delta x_{i+1/2}} A_{i+1/2,j}, \\ R^s_{i,j} &= \frac{g\Delta t^2\theta^2}{a^\tau_{i,j}\Delta y_{j-1/2}} A_{i,j-1/2}, \quad R^n_{i,j} = \frac{g\Delta t^2\theta^2}{a^\tau_{i,j}\Delta y_{j+1/2}} A_{i,j+1/2}.\end{aligned} \tag{30}$$

To solve Eq. (29), boundary conditions for $\Delta\eta$ need to be specified. Depending on the boundary type and data used for the open boundaries, the boundary conditions can be either a Dirichlet-type or a Neumann-type. If it is an open boundary grid where the water level is known, the Dirichlet-type boundary condition is used: $\Delta\eta = \eta^{n+1} - \eta^n$. If it is an open boundary where the flow rate is given or if it is a solid boundary, the Neumann-type boundary condition is used with a zero gradient of $\Delta\eta$ in the normal direction.

Starting from the southwest corner of the computation domain and doing a 2-D loop (saying the i-loop is the internal loop), Eq. (29) can be written for each cell, forming a five-diagonal matrix system with a known right-hand side after the first step is done. To save space, the five diagonals can be saved in five 1-D arrays using an index $l = (j-1)N_x + i$, where N_x is the total number of grids in the x-direction. As can be seen from Eq. (30), R^w, R^e, R^s, and R^n are all positive. If a uniform grid system is used, then $R^e_{i,j} = R^w_{i+1,j}$ and $R^n_{i,j} = R^s_{i,j+1}$, or the five-diagonal system is symmetric. In this case, the five-diagonal matrix system is positive definite. The most efficient way to solve this kind of matrix system is the conjugate gradient method. For faster convergence, incomplete Cholesky preconditioning [11] can be used in the conjugate gradient method. If a non-uniform grid system is used, then the five-diagonal system is generally non-symmetric. One can use the bi-conjugate gradient stabilized (Bi-CGSTAB) method [12] that provides relatively uniform convergence for non-symmetric matrices. The solution of (29) gives the final free surface location. The final velocity field can then be calculated by solving Eqs. (21) and (22) and the continuity equation. Eqs. (21) and (22) are tri-diagonal systems which are easy to solve. In a real computation, however, there is actually no need to solve the tri-diagonal systems of Eqs. (21) and (22). Note that the vertical eddy viscosity terms in Eqs. (21) and (22) disappear in Eqs. (23) and (24). This is because the vertical integration of Eqs. (21) and (22) cancels the shear stresses between the horizontal layers and the boundary conditions at the free surface and the bottom are the same for both the final and intermediate velocities. Therefore, the eddy viscosity terms in Eqs. (21) and (22) have no effect on the derivation of Eqs. (28) and (29). Clearly, δu and δv in the following expressions satisfy Eqs. (21) and (22) with the boundary conditions $\partial(\delta u)/\partial z = \partial(\delta v)/\partial z = 0$ at the free surface and the bottom:

$$\delta u = -\Delta tg\theta \frac{\partial \Delta\eta}{\partial x}, \tag{31}$$

$$\delta v = -\Delta tg\theta \frac{\partial \Delta\eta}{\partial y}. \tag{32}$$

Because the right-hand sides of Eqs. (31) and (32) do not depend on z, neither δu nor δv are a function of z-coordinate. The final velocity distribution in the vertical direction is simply shifted from its intermediate one with a displacement, which is negatively proportional to the horizontal gradient of free surface change over the time step Δt. It should be mentioned that because δu and δv expressed in Eqs. (31) and (32) are invariant of the z-coordinate, they always satisfy Eqs. (21) and (22) no matter what kind of model is used for the vertical eddy viscosity (A_v), simply because $\partial(\delta u)/\partial z = \partial(\delta v)/\partial z \equiv 0$ for the entire water column. The model provides several options for the estimation of the vertical eddy viscosity, including a simplified second-order closure model and a turbulent kinetic energy [13] that is similar to that of Sheng and Villaret [14].

After the flow field is solved, the model uses the following flux-based finite difference scheme to solve the transport equation expressed in Eq. (10):

$$\begin{aligned}\frac{\Phi^{n+1}_{i,j,k} - \Phi^{n}_{i,j,k}}{\Delta t} = S_s + \frac{1}{V^n_{i,j,k}}\Bigg[&\Delta F^n_x + \Delta F^n_y + \Delta F^n_z + \Delta f^n_x + \Delta f^n_y + a^n_{i,j,k+1/2} B^n_{v_{i,j,k+1/2}} \frac{\Phi^{n+1}_{i,j,k+1} - \Phi^{n+1}_{i,j,k}}{\Delta z^n_{k+1/2}} \\ &- a^n_{i,j,k-1/2} B^n_{v_{i,j,k-1/2}} \frac{\Phi^{n+1}_{i,j,k} - \Phi^{n+1}_{i,j,k-1}}{\Delta z^n_{k-1/2}}\Bigg],\end{aligned} \tag{33}$$

where $V^n_{i,j,k}$ is the water volume of the cell (varies with time for the top cell), ΔF^n_x, ΔF^n_y, and ΔF^n_z represent explicit discretizations of net advective fluxes of the material flowing into cell (i, j, k) in the x-, y-, and z-directions, respectively, and Δf^n_x and Δf^n_y are net diffusive fluxes of the concentration entering the cell from the x- and y-directions, respectively. Eq. (33) is a tri-diagonal system and can be easily solved by the Thomas Algorithm.

3. Implementation of the FSC method

It should be pointed out that there is no need to calculate the intermediate vertical velocity (w^{n+*}), because it is not involved in the calculations in the second step. Also, the use of the Leibnitz integration law to separate pressure gradients into baroclinic and barotropic components in the last section is just for the purpose of explaining the FSC method. In real computation, due to the explicit treatment of the baroclinic term, it is not needed to separate the two pressure components, and the following equations are solved to obtain the intermediate velocities:

$$\frac{u^{n+*}-u^n}{\Delta t} = fv^n - \frac{1}{\rho_0}\frac{\partial p^n}{\partial x} + H_x^n + \frac{\partial}{\partial z}\left(A_{\mathrm{v}}\frac{\partial u^{n+*}}{\partial z}\right), \tag{34}$$

$$\frac{v^{n+*}-v^n}{\Delta t} = -fu^{n+*} - \frac{1}{\rho_0}\frac{\partial p^n}{\partial y} + H_y^n + \frac{\partial}{\partial z}\left(A_{\mathrm{v}}\frac{\partial v^{n+*}}{\partial z}\right). \tag{35}$$

Furthermore, when the FSC method was coded in the model, volume-averaged values are used for the pressure gradient terms:

$$\frac{\partial p^n}{\partial x} = \frac{1}{\mathcal{V}^n_{i+1/2,j,k}}\int\int\int_{\mathcal{V}^n_{i+1/2,j,k}} \frac{\partial p^n}{\partial x}\,\mathrm{d}\mathcal{V}, \tag{36}$$

$$\frac{\partial p^n}{\partial y} = \frac{1}{\mathcal{V}^n_{i,j+1/2,k}}\int\int\int_{\mathcal{V}^n_{i,j+1/2,k}} \frac{\partial p^n}{\partial y}\,\mathrm{d}\mathcal{V}, \tag{37}$$

where $\mathcal{V}^n_{i+1/2,j,k}$ is the volume of the east half of cell (i, j, k) plus the volume of the west half of cell ($i+1$, j, k), and $\mathcal{V}^n_{i,j+1/2,k}$ is the volume of the north half of cell (i, j, k) plus the volume of the south half of cell (i, $j+1$, k). H_x^n and H_y^n in Eqs. (34) and (35), on the other hand, take the following forms:

$$\begin{aligned} H_x^n = {} & \frac{1-\alpha}{\mathcal{V}^n_{i,j,k}}(\mathbf{I}^n_{i,j,k} + XX^n_{i+1/2,j,k} - XX^n_{i-1/2,j,k} + YX^n_{i,j+1/2,k} - YX^n_{i,j-1/2,k}) \\ & + \frac{\alpha}{\mathcal{V}^n_{i+1,j,k}}(\mathbf{I}^n_{i+1,j,k} + XX^n_{i+3/2,j,k} - XX^n_{i+1/2,j,k} + YX^n_{i+1,j+1/2,k} - YX^n_{i+1,j-1/2,k}), \end{aligned} \tag{38}$$

$$\begin{aligned} H_y^n = {} & \frac{1-\beta}{\mathcal{V}^n_{i,j,k}}(\mathbf{J}^n_{i,j,k} + XY^n_{i+1/2,j,k} - XY^n_{i-1/2,j,k} + YY^n_{i,j+1/2,k} - YY^n_{i,j-1/2,k}) \\ & + \frac{\beta}{\mathcal{V}^n_{i,j+1,k}}(\mathbf{J}^n_{i,j+1,k} + XY^n_{i+1/2,j+1,k} - XY^n_{i-1/2,j+1,k} + YY^n_{i,j+3/2,k} - YY^n_{i,j+1/2,k}), \end{aligned} \tag{39}$$

where $\alpha = 0.5\Delta x_i/(\Delta x_i + \Delta x_{i+1})$, $\beta = 0.5\Delta y_i/(\Delta y_j + \Delta y_{j+1})$, $\mathbf{I}^n_{i,j,k}$ and $\mathbf{J}^n_{i,j,k}$ are, respectively, the net u-momentum flux and v-momentum flux entering cell (i, j, k) from three directions, $XX^n_{i+1/2,j,k}$ and $XY^n_{i+1/2,j,k}$ are integrations of $A_{\mathrm{h}}\partial u/\partial x$ and $A_{\mathrm{h}}\partial v/\partial x$, respectively, over the east face of cell (i, j, k), while $YY^n_{i,j+1/2,k}$ and $YX^n_{i,j+1/2,k}$ are integrations of $A_{\mathrm{h}}\partial v/\partial y$ and $A_{\mathrm{h}}\ \partial u/\partial y$, respectively, over the north face of the cell.

The FSC method described above can be conveniently implemented in 3-D hydrodynamic models for free-surface flows. The implementation of the two steps is summaried below. The first step includes the following sub-steps:

1. Calculate hydrostatic pressure using Eq. (4) and free surface at the previous time step.
2. Calculate horizontal pressure gradients.

3. Calculate A_h and A_v using proper turbulence models.
4. Calculate H_x and H_y using Eqs. (38) and (39).
5. Solve Eqs. (34) and (35) with the Thomas Algorithm to get intermediate horizontal velocities (u^{n+*} and v^{n+*}).
6. Calculate the intermediate free surface (or $\Delta\eta^*_{i,j}$) using Eq. (17).

In the second step, the following sub-steps are carried out:

1. Calculate R^w, R^e, R^s, and R^n using Eq. (30) to form a five-diagonal matrix system.
2. Solve Eq. (29) to get the final free surface using the conjugate gradient method with incomplete Cholesky preconditioning or the bi-conjugate gradient stabilized (Bi-CGSTAB) method.
3. Calculate horizontal gradients of the final free-surface increment in the x- and y-directions.
4. Calculate velocity corrections using Eqs. (31) and (32) and get the final horizontal velocities.
5. Calculate final vertical velocity using the continuity equation similar to Eq. (16) (replace $n+*$ with $n+1$ in the equation).

All sub-steps in the above two time steps can be performed straightforwardly, except for sub-step (2) of the second step that is somewhat time-consuming because a five-diagonal system has to be solved. Comparing to the semi-implicit method in Casulli and Cheng [6] and Casulli and Stelling [8] and the implicit method in Namin et al. [24], the formation of the five-diagonal matrix in the FSC method is much simpler. The FSC method decouples the implicit treatment of the vertical eddy viscosity terms from the semi-implicit treatment of the barotropic terms. As a result, the calculation of the free-surface location in the FSC method is simpler than that in [6,8]. Unlike the semi-implicit method in [6,8] or the implicit method in [24], there is no matrix calculation involved in computing the coefficients of the five-diagonal system of Eq. (29). Therefore, the formation of the five-diagonal matrix in the FSC method is quite simple. Although an extra step is needed to correct the intermediate velocity field, such a correction can be easily done using Eqs. (31) and (32).

4. Properties of the FSC method

Because the five-diagonal matrix system for the free-surface change over Δt is derived from the vertically integrated continuity equation, the method is mass conservative both locally and globally. Although the explicit discretization of barotrpic terms in the first step only allows a very small time step restricted by the celerity of the external gravity wave, the correction of the free surface eliminates this time step restriction. Following the same procedure described in Abbott and Basco [15], a stability analysis can be done and shows that when $\theta \geqslant 0.5$, the FSC method is unconditionally stable with respect to the external gravity wave. The numerical scheme is also unconditionally stable with respect to bottom stresses and vertical eddy viscosity terms because of the implicit treatment of these terms. The explicit treatment of the horizontal eddy viscosity terms requires that the time step not to exceed $\Delta x^2\ \Delta y^2/(2A_h)/(\Delta x^2 + \Delta y^2)$, while the stability condition for the Coriolis terms is $\Delta t \leqslant 1/f$. In lake and estuarine simulations, these two constraints are relatively mild as compared to the time step restriction imposed by the explicit treatment of the convective terms that requires the time step not to exceed $(|u_{\max}|/\Delta x + |v_{\max}|/\Delta y)^{-1}$. For stratified flows, the explicit treatment of the baroclinic terms leads to a time step constraint that is controlled by the propagation speed of an internal wave ($c_b = \sqrt{g'D}$, where g' is the reduced gravity due to stratification and D is the water depth), or $\Delta t \leqslant \Delta x/c_b$. For the advection–diffusion equation, the explicit advection terms also impose a time step limit of $(|u_{\max}|/\Delta x + |v_{\max}|/\Delta y)^{-1}$. The time step constraint due to the explicit discretization of the horizontal diffusion terms is $\Delta t \leqslant \Delta x^2\Delta y^2/(2B_h)/(\Delta x^2 + \Delta y^2)$.

It should be pointed out that although the FSC method is unconditionally stable with respect to the gravitational wave when θ is greater than 0.5, it is dissipative for $\theta > 0.5$. The highest dissipation occurs when $\theta = 1$. To obtain model results that are non-dissipative, one has to use a θ value of 0.5 [16].

It can be seen that when $\theta = 0$, Eq. (29) is reduced to $\Delta\eta_{i,j} = \Delta\eta^*_{i,j}$ and there is no need to solve Eq. (29) because the final free-surface elevation ($\eta^{n+1}_{i,j}$) is the same as the intermediate free surface elevation ($\eta^{n+*}_{i,j}$). As a result, the velocity corrections ($\delta u, \delta v$) are zero and there is actually no need to carry out the second step of the FSC method at all. However, when $\theta = 0$, the model is unstable if $\eta^{n+*}_{i,j}$ is calculated from Eq. (17), because both the horizontal gradients of the free surface in the momentum equations and the horizontal fluxes in the vertically integrated continuity equation are discretized explicitly and a negative numerical diffusion is involved [16]. Since the intermediate velocity field (u^{n+*}, v^{n+*}) is already available before the second step is carried out, the model uses (u^{n+*}, v^{n+*}) instead of (u^n, v^n) to calculate $\eta^{n+*}_{i,j}$ if $\theta = 0$. The resulting numerical model is stable when $\Delta t \leqslant \Delta x/\sqrt{gD}$. Therefore, when $\theta = 0$, the model treats the horizontal gradients of the free surface in the momentum equations explicitly, but uses the newest velocity field to calculate the fluxes in the vertically integrated continuity equation.

Time differencing in the FSC method is at least first-order accurate. The staggered arrangement of model variables (Fig. 1) allows pressure gradient terms and eddy viscosity terms to be easily discretized with the central differencing scheme that has a second-order accuracy in space, or $O(\Delta x^2)$. The accuracy of the convective terms depends on the finite difference scheme used in the simulation. The model provides several choices for the explicit treatments of convective/advective terms, including the standard upwind differencing, central differencing, combined upwind-central differencing, QUICK (Quadratic Upstream Interpolation for Convective Kinematics), QUICKEST (QUICK with Estimated Streaming Terms) [17], and a flux limiting scheme using Roe's superbee limiter [18], etc. The standard upwind scheme, for example, is accurate only to the first order, while the QUCKEST scheme has a third-order accuracy, or $O(\Delta x^3)$.

5. Test of the FSC method

The FSC method was first validated with various idealized cases, including checking mass conservations for simple and complex bathymetries. This section shows two of the test cases. A model application to a real estuary is described in the next section.

In the first test case, two seiche oscillations in a rectangular basin with a constant depth (D) of 5 m were simulated. The horizontal dimension of the basin is 120 m in the x-direction and 60 m in the y-direction. At time = 0, the water has no velocity, but has a free surface setup in the following form:

$$\eta = a\cos\left(\frac{\pi x}{L_x}\right)\cos\left(\frac{\pi y}{L_y}\right), \tag{40}$$

where $L_x = 120$ m, $L_y = 60$, a is 2 cm for the first oscillation and 30 cm for the second oscillation. The southwest corner of the basin is the origin for both the x- and y-coordinates and the center of the basin is at $x = 60$ m and $y = 30$ m. For this kind of 3-D seiching problem, the linear wave theory gives the following first-order analytical solutions:

$$\begin{aligned}
\eta &= a\cos\left(\frac{\pi x}{L_x}\right)\cos\left(\frac{\pi y}{L_y}\right)\cos(\sigma t),\\
(u,v) &= \frac{ag\pi}{\sigma}\frac{\cosh(k_w z)}{\cosh(k_w D)}\left(\frac{1}{l_x}\sin\left(\frac{\pi x}{L_x}\right)\cos\left(\frac{\pi y}{L_y}\right), \frac{1}{l_y}\cos\left(\frac{\pi x}{L_x}\right)\sin\left(\frac{\pi y}{L_y}\right)\right)\sin(\sigma t),\\
w &= -\frac{agk}{\sigma}\frac{\sinh(k_w z)}{\cosh(k_w D)}\cos\left(\frac{\pi x}{L_x}\right)\cos\left(\frac{\pi y}{L_y}\right)\sin(\sigma t),
\end{aligned} \tag{41}$$

where $\sigma = k_w\sqrt{gD}$, $k_w = \pi\sqrt{L_x^{-2} + L_y^{-2}}$, and the origin of the z-coordinate is at the bottom of the basin.

Both seiche oscillations were simulated with a total of 36,864 grid cells (62, 32, and 18 cells in the x-, y-, and z-directions, respectively). While a uniform grid spacing of 0.3 m is used in the z-direction, Δx and Δy vary between 0.2 and 2 m in the horizontal directions. In both seiche simulations, eddy viscosities in three directions were set to zero. Both the bottom friction and wind shear stress were assumed to be zero. The QUICKEST scheme for convective terms was chosen in model runs with a time step of 0.25 s.

Figs. 2 and 3 show comparisons of model results (solid lines) with analytical solutions (dashed lines) expressed in Eq. (41) for the first and second seiche oscillations, respectively. While Fig. 2 compares model results with analytical solutions for the first oscillation case with the amplitude of 2 cm, Fig. 3 are comparisons for the second oscillation case with the amplitude of 30 cm. In Figs. 2 and 3, surface elevations are plotted in top graphs 2(a) and 3(a), while u-, v-, and w-velocities are plotted in 2(b) and 3(b), 2(c) and 3(c), and 2(d) and 3(d), respectively. Thick lines are results for a location near a corner of the basin with the horizontal coordinates of $(x, y) = (0.25\text{ m}, 0.25\text{ m})$, while thin lines are those near the center of the basin with the coordinates of $(x, y) = (65.5\text{ m}, 35.5\text{ m})$. In Figs. 2 and 3, all velocities are compared at a level that is 3.15 m above the bottom, or $z = 3.15$ m.

From Fig. 2, it can be seen that simulated surface elevations and u-, v-, and w-velocities agree very well with the first-order analytical solutions for the first seiche oscillation, which has a small amplitude and very weakly nonlinear terms. For the second seiche oscillation, Fig. 3 shows that model results at the two locations deviate from the first-order analytical solutions as time goes on. The reason for this deviation is that the linear wave theory is only valid for small amplitude waves because the nonlinear terms (convection terms) are negligible for small amplitude waves. For a finite amplitude wave such as the second seiche oscillation, the nonlinear terms cannot be neglected and the solutions given in Eq. (41) are not valid anymore. As can be seen from Fig. 3, higher mode oscillations are generated by the nonlinear terms as time goes on.

The second idealized test case is the development of a 3-D eddy caused by a combination of the Coriolis force and the baroclince force. Griffiths and Linden [19] conducted a laboratory experiment, in which a bottomless cylinder of less dense water is placed at the middle of a rotating tank containing dense water. At $t = 0$, the cylinder was removed. They found that the less dense water initially rises and spreads rapidly outwards in the upper layer. While the water in the upper layer flows outwards, the water in the lower layer flows inwards. Under the Colioris effect, an anticyclonical flow pattern in the upper layer and a cyclonical flow pattern in the lower layer were observed. James [20] and Tartinville et al. [21] conducted numerical experiments similar to the laboratory experiment conducted by Griffiths and Linden, but for an idealized square basin that is 20 m deep and 30 km wide. Although a much larger horizontal length scale was used, James [20] and Tartinville et al. [21] were able to simulate the 3-D flow pattern found by Griffiths and Linden in the laboratory. To test the FSC method this study used a square basin with a width of 45.5 km and a constant depth of 20 m. The setup of the model test was the same as that in Tartinville et al. [21]. Again, there was no wind acting on the free surface and the bottom friction and eddy viscosities were set to zero. The QUICKEST scheme was used for convective and advective terms. The model was run from the cold start with the following initial salinity distribution:

$$\Phi = \begin{cases} 33.75 + 1.1\left[\frac{R}{3}\right]^8, & R \leqslant 3\text{ km and } 10\text{ m} < z \leqslant 20\text{ m}, \\ 34.85, & \text{elsewhere}, \end{cases} \tag{42}$$

where R is the distance measured from the center (looking from above) of the basin and z is the distance from the bottom. Assuming that the latitude is 30° N, the Coriolis parameter is $f = 7.29212 \times 10^{-5}\ \text{s}^{-1}$.

The vertical spacing used for the simulation was 1 m, while the horizontal grid size varied from 0.5 (near the center) to 2 km (near the sidewall). The model was run for 96 h with a time step of 150 s. Fig. 4 shows velocity and salinity distributions at the top (19.5 m above the bed) and bottom (0.5 m above the bed) layers at $t = 1$, 5, 48, and 96 h. Side (x–z) views of velocity fields and salinity distributions along a transect parallel to the x-axis through the center of the basin are shown in Fig. 5. For clarity, the four graphs in Fig. 4 only shows results within the range of $15\text{ km} < x < 30.5\text{ km}$ and $15\text{ km} < y < 30.5\text{ km}$, while Fig. 5 only shows

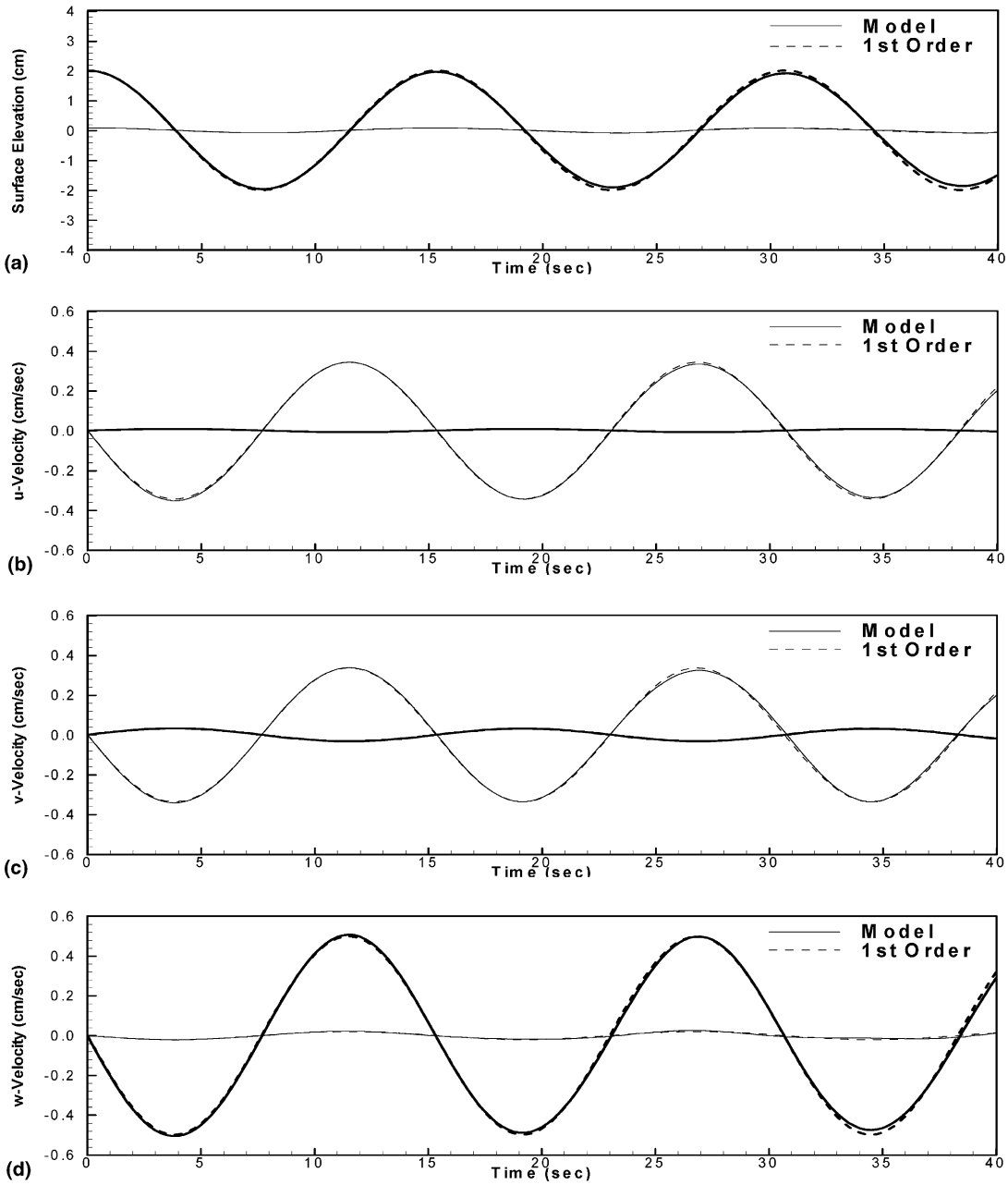

Fig. 2. Comparisons of simulated surface elevations, u-, v-, and w-velocities with the first-order analytical solutions according to the linear wave theory for the first 3-D seiche case in a rectangular basin with a constant depth of 5 m. The amplitude is 2 cm. Thick lines are comparisons at a location near a corner of the basin, while thin lines are near the center of the basin.

results within the range of 12 km $< x <$ 33.5 km. Comparing Figs. 4 and 5 with what were found in the laboratory experiment [19] and previous numerical simulations [20,21], model results using the FSC method are consistent with previous studies. During the first couple of hours, an upwelling near the center of the

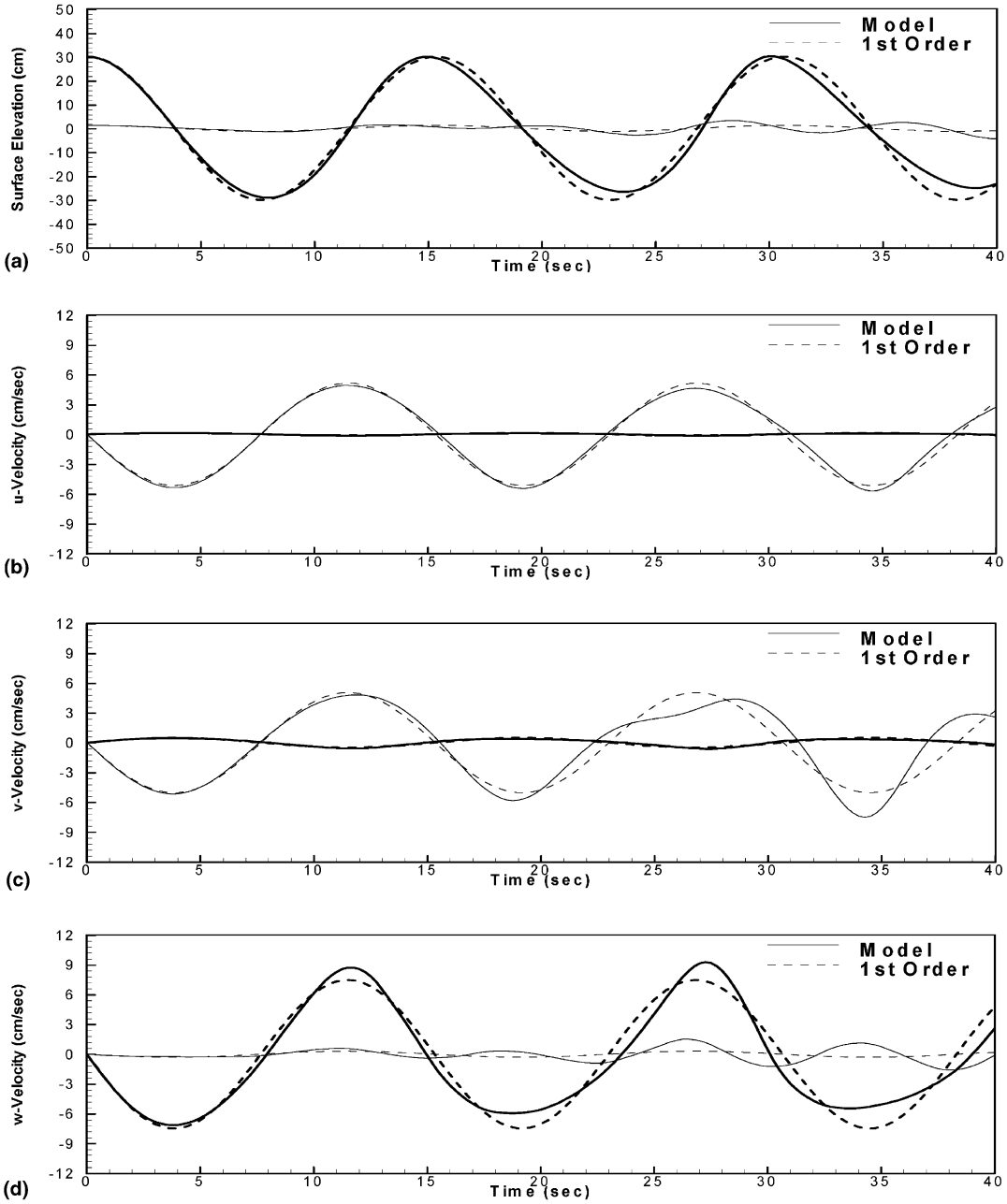

Fig. 3. Comparisons of simulated surface elevations, u-, v-, and w-velocities with the first-order analytical solutions according to the linear wave theory for the first 3-D seiche case in a rectangular basin with a constant depth of 5 m. The amplitude is 30 cm. Thick lines are comparisons at a location near a corner of the basin, while thin lines are near the center of the basin.

basin can be seen in Fig. 5, along with a rapid outward spread of less dense water in the upper layer and an inward flow pattern in the lower layer. Under the Coriolis influence, the outward flow forms a clockwise eddy rotating anticyclonically in the top layer, while the inward flow becomes a counterclockwise eddy

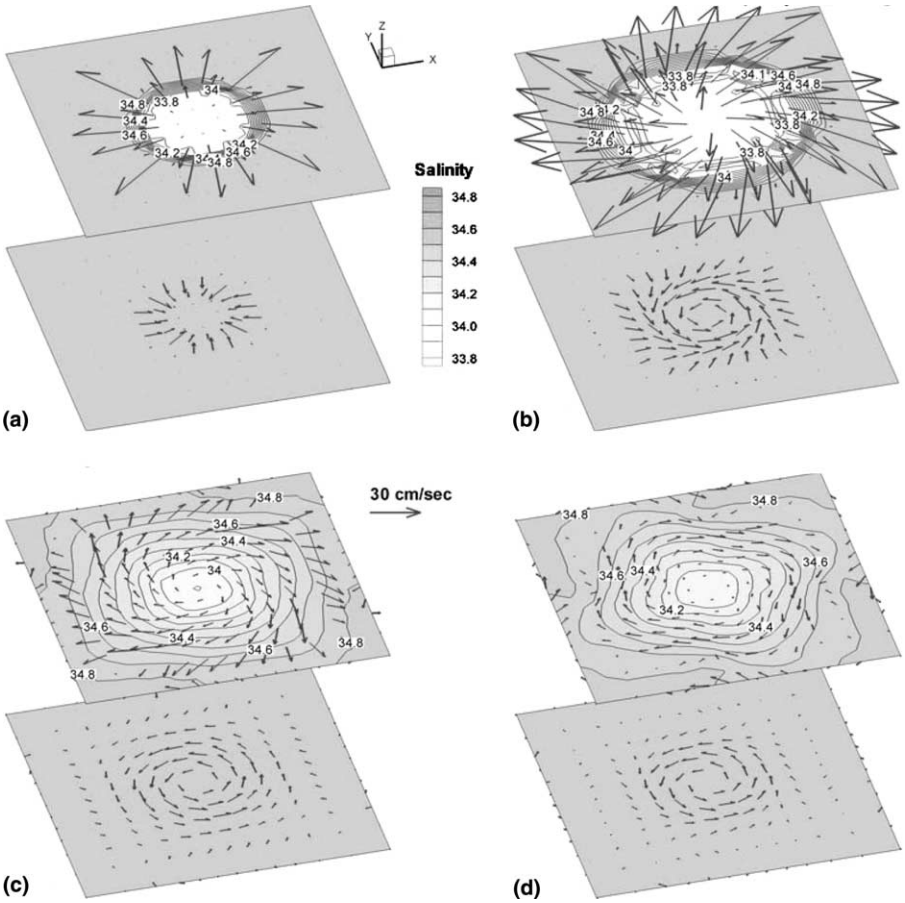

Fig. 4. Three-dimensional views of simulated velocity fields and salinity contours at the top and bottom layers at $t = 1$ h (a), 5 h (b), 48 h (c), and 96 h (d) during the development of an eddy.

rotating cyclonically in the bottom layer. Although not showing in Figs. 4 and 5, simulated eddies using the FSC method oscillate with a frequency that is proportional to f. This is also consistent with the laboratory observations by Griffiths and Linden [19].

6. Application to a real estuary

The FSC method presented here was applied to the estuarine portion of the Alafia River in southwest Florida (Fig. 6). The river is narrow and meandering except for its most downstream 4 km where it is wider and has a few islands. There are five USGS (United States Geological Survey) continuous recording stations along the Alafia River. The USGS has been measuring data at the Alafia River at Gibsonton station since early 1990s, but continuous data recordings at the other stations did not start until a few years ago. The most complete data available for the model application were collected since May 1999, except for the Alafia River near Gibsonton station where data collection began in early November 1999. Surface elevation and salinity data were collected at 15-min intervals at four downstream stations shown in Fig. 6. At the most upstream station (Alafia River at Lithia) located about 24 km upstream from the

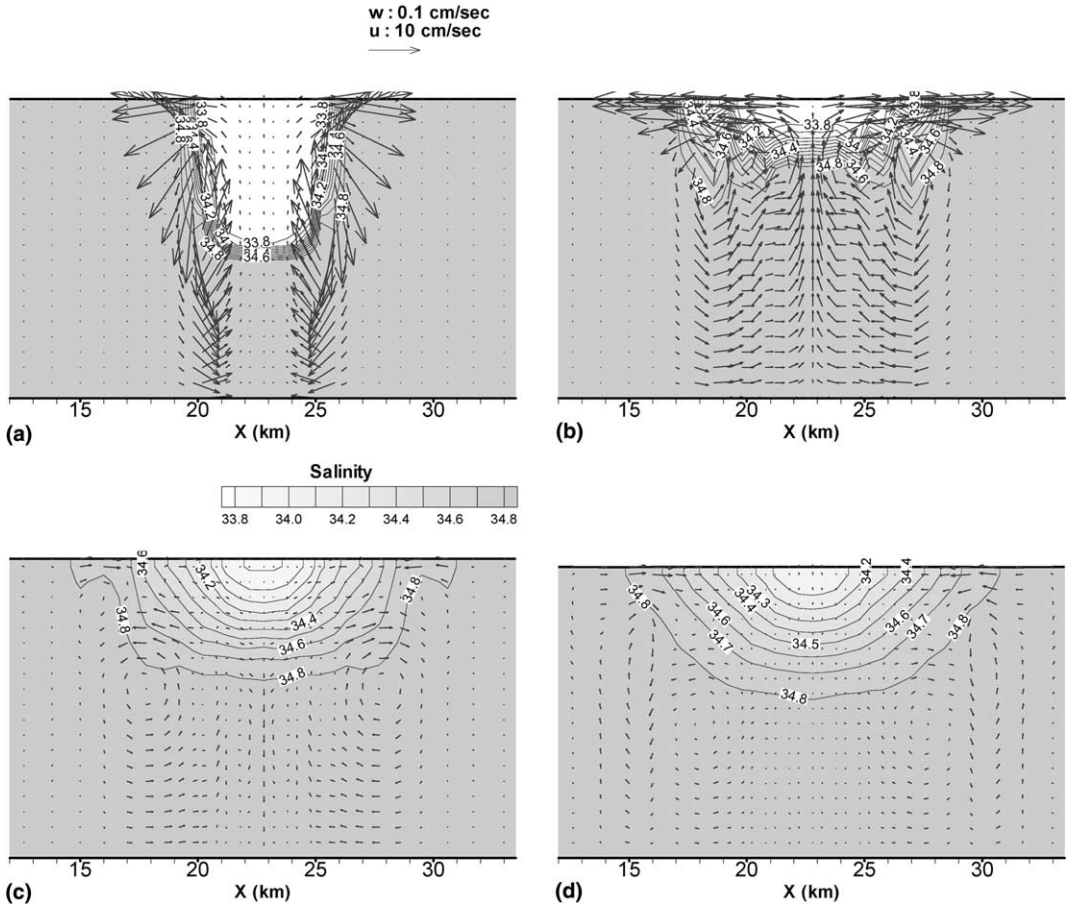

Fig. 5. Simulated velocity fields and salinity distributions along a transect parallel to the x-axis and through the center of the basin at $t = 1$ h (a), 5 h (b), 48 h (c), and 96 h (d) during the development of an eddy.

mouth, only flow was measured, because no tidal signal is detected there. Normally, tide can be observed at about 18 km upstream from the mouth, although saline water is usually limited only to the downstream 12 km.

Due to the physical configuration of the river, hydrodynamics in the river was first simulated with a laterally averaged 2-D model using the FSC method [22] for the entire reach of 24 km from the mouth (Alafia River at Gibsonton) to Alafia River at Lithia. The 3-D FSC scheme presented here was used for the most downstream 4.5 km of the river, from the mouth to about 850 m downstream from Highway 301 (Fig. 6). Measured surface elevation, velocity, and salinity at four locations shown in Fig. 6 were used for the boundary conditions and for calibrations/verifications of the 2-D and 3-D models. While the downstream boundary conditions for 3-D runs are the same as those for the 2-D runs, the upstream boundary conditions used in 3-D runs are simulated 2-D model results.

Although the computational domain for the 3-D simulation is just 4.5 km long, flow in this river segment is quite nonlinear because of the presence of islands and some shallow areas where the wetting/drying process occurs during the tidal cycle. The model handles the wetting and drying by updating and bookkeeping actual water volumes and side and top areas of each top cells at each time step. If the water volume is zero for a water column with the horizontal grid indexes of (i, j), then grid (i, j) is a dry grid.

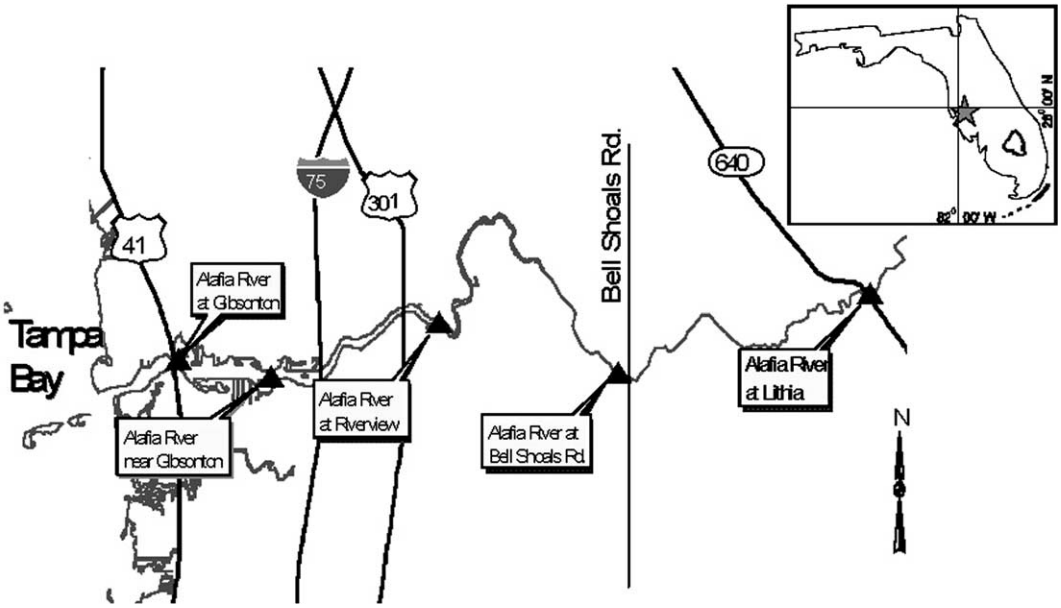

Fig. 6. Alafia River flows to Tampa Bay in southwest Florida. There are five USGS continuous recording stations along the river.

Otherwise, it is a wet grid. Nevertheless, when the computation marches from one time step to the next time step, a wet grid is not necessarily a computation grid. In other words, it may not be included in the computation during that time stepping process. The criterion for the model to determine if a wet grid is a computation grid or not at each time step is that the water level at the center of the grid should be higher or equal to the middle point of k_nth layer, where k_n is the k-index of the bottom layer for the horizontal grid (i, j). For a wet horizontal grid that is not included in the computation, its surface elevation and concentrations are estimated using the averaged values of its neighboring computation grids that are directly connected to it:

$$\bar{\eta} = \frac{1}{N_n}\sum_{l=1}^{N_n}\eta_l^{n+1}, \quad \bar{\Phi} = \frac{1}{N_n}\sum_{l=1}^{N_n}\Phi_l^{n+1}, \tag{43}$$

where $\bar{\eta}$ and $\bar{\Phi}$ are averages of surface elevations and concentrations of the neighboring computation grids, which are labeled with the subscript l, and N_n is the total number of the neighboring computation grids. To ensure mass conservations, final results of all grids involved need to be corrected:

$$\begin{aligned} &\eta_l^{n+1} \Leftarrow \eta_l^{n+1} - \delta\eta^*, \quad \Phi_l^{n+1} \Leftarrow \Phi_l^{n+1} - \delta\Phi^*, \\ &\eta_0^{n+1} \Leftarrow \bar{\eta} - \delta\eta^*, \quad \Phi_0^{n+1} \Leftarrow \bar{\Phi} - \delta\Phi^*, \end{aligned} \tag{44}$$

where the symbol $\Leftarrow$ means replacing the left-hand side with the right-hand side, the subscript 0 denotes the wet grid that is not computed and needs to be estimated, $\delta\eta^*$ and $\delta\Phi^*$ are corrections and take the following forms:

$$\delta\eta* = \frac{(\bar{\eta} - \eta_{i,j}^n)a_0^n}{a_t}, \quad \delta\Phi = \frac{[\mathcal{V}_0^n + (\eta_0^{n+1} - \eta_0^n)a_0^n]\Phi_0^{n+1} - \mathcal{V}_0^n\Phi_0^n}{\mathcal{V}_t}, \tag{45}$$

where a_0^n and $\mathcal{V}_0^n$ are, respectively, the surface water area (the actual wet surface area) and water volume of the wet grid whose surface elevation and concentrations need to be estimated, a_t and $\mathcal{V}_t$ are sums of water

surface areas (actual wet surface areas) and water volumes of all grids involved in the estimation, including the neighboring computation grids and the wet grid whose surface elevation and concentrations need to be estimated.

The computational domain of the Lower Alafia River was discretized with a horizontal mesh of $\Delta x = 100$ m and $\Delta y = 60$ m and a vertical spacing $\Delta\zeta$ varying between 0.3 and 0.5 m. Numbers of grids in the x-, y-, and z -directions are 45, 18, and 12, respectively, resulting in a total of 9720 grid cells. The length of the simulation was a 320-day period from May 10, 1999 to March 24, 2000. The time step used for the 3-D model runs was $\Delta t = 150$ s. The model was run on a Pentium III single CPU of 933 MHz. The 320-day simulation of hydrodynamics and salt transport processes took about 213 min of CPU time to complete.

Fig. 7 shows comparisons of simulated surface elevation and salinity with measured data at the USGS Alafia River near Gibsonton station, where the salinity was measured at a depth of about 30 cm above the bed. For simplicity, only results during the last 20 days of the simulation are shown in the figure. As can be seen from Fig. 7, the FSC scheme presented here yielded reasonably good model results that agree well with measured field data.

Figs. 8 and 9 are 3-D plots of velocity fields and salinity distributions at time = 7538.0 and 7548.0 h, respectively. The former is at a high water level during the ebb tide, while the latter is at a lower water level during the flood tide. Grey scales in Figs. 8 and 9 represent different salinity ranges shown in the legend. Closed areas inside the river are three small islands that are partially submerged when the water level is high

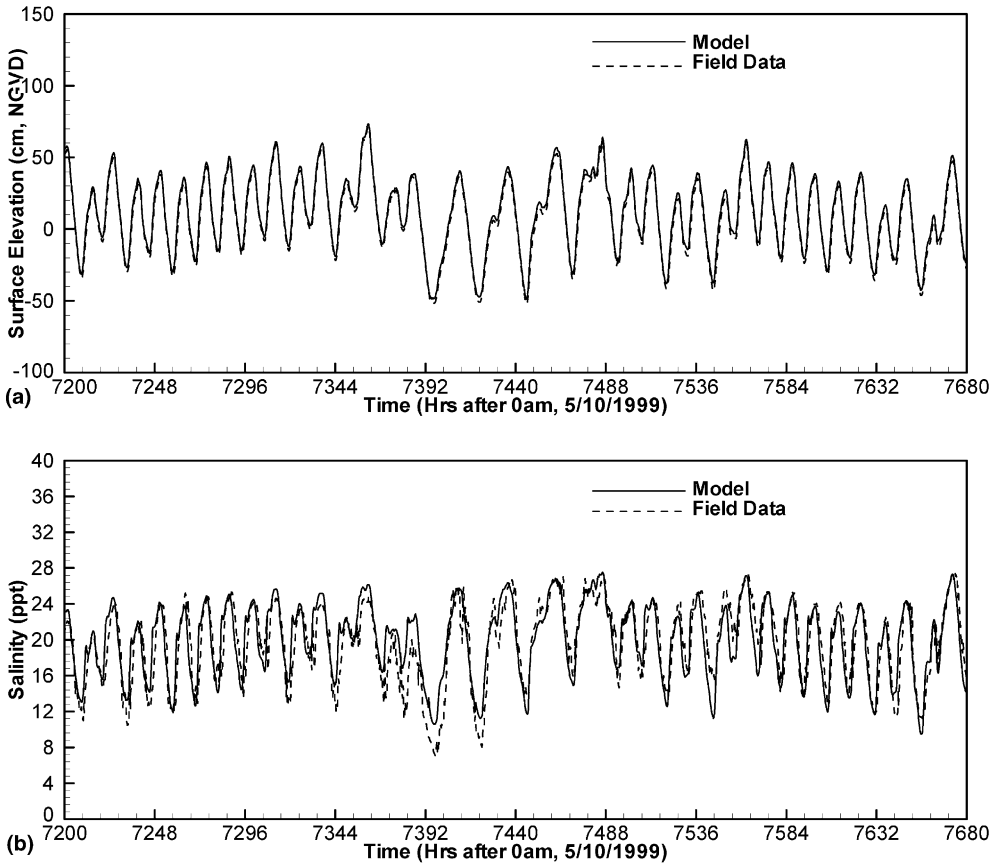

Fig. 7. Comparison of simulated and measured surface elevations (a) and salinities (b) during a 20-day period in the lower portion of the Alafia River, southwest Florida.

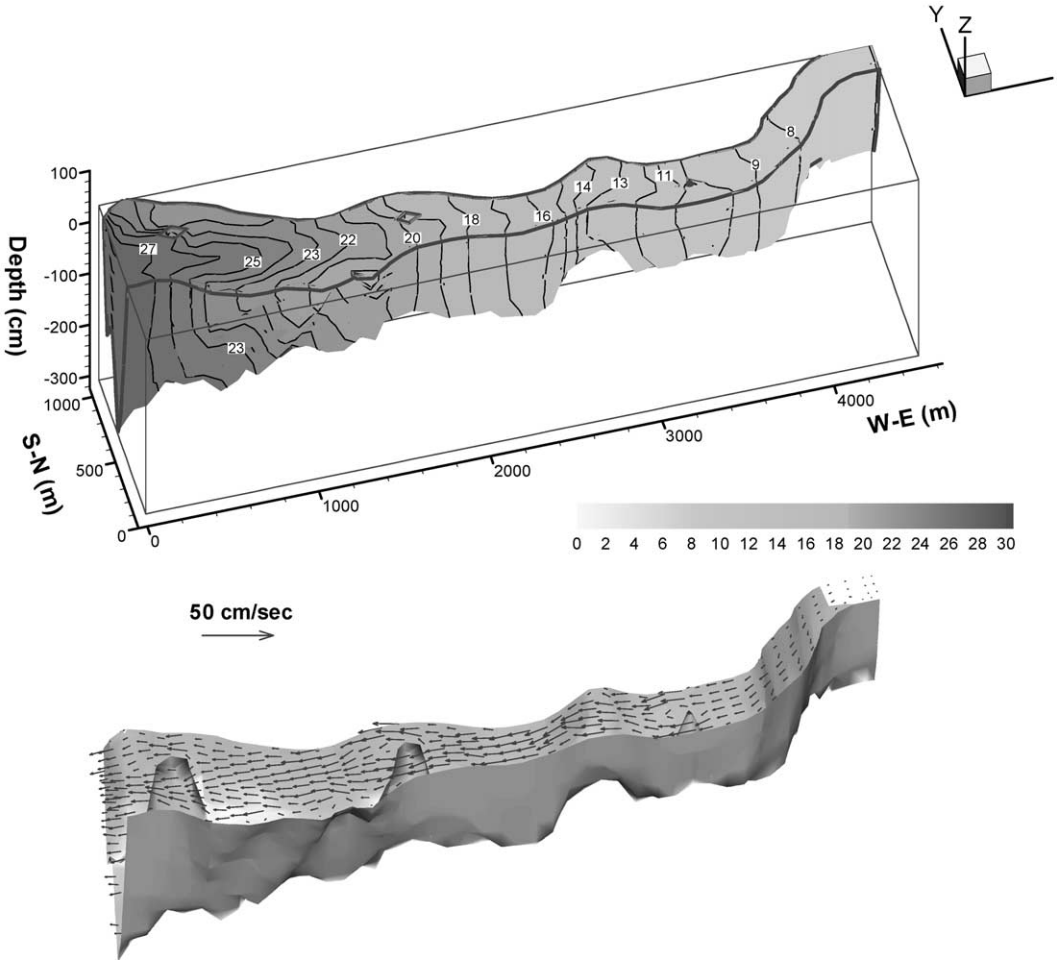

Fig. 8. Simulated velocity and salinity distributions in the Lower Alafia River at time = 7538.0 h when the water level is high during the ebb tide.

and emerged when the water level is low. A comparison of shorelines in Figs. 8 and 9 indicates that the wetting/drying process is well handled by the model. Because of a low water level, emerged areas of the islands in Fig. 9 are larger than those in Fig. 8. Near the south bank at about 1 km from the downstream boundary, a shallow area is submerged in Fig. 8, but exposed to the air in Fig. 9. Both Figs. 8 and 9 show that flow fields and salinity distributions in the lower portion of the Alafia River pattern are 3-D due to the existence of islands and some shallow areas.

The averaged water depth in the lower portion of the river is about 2 m, with the deepest area being just 3.25 m deep. The celerity of the gravitational wave estimated from the depth data varies around 5 m/s. With a horizontal grid size of 60 m in the y-direction, the time step used in the simulation would be, according to the CFL condition for gravity waves, restricted to 12 s or shorter if the explicit discretization were used in the model and the second step of the FSC method were not performed. Nevertheless, the free-surface correction step in the FSC method eliminates such time step restriction. As a result, a much larger time step, which is more than one order of magnitude longer, is allowed in model runs without any problems.

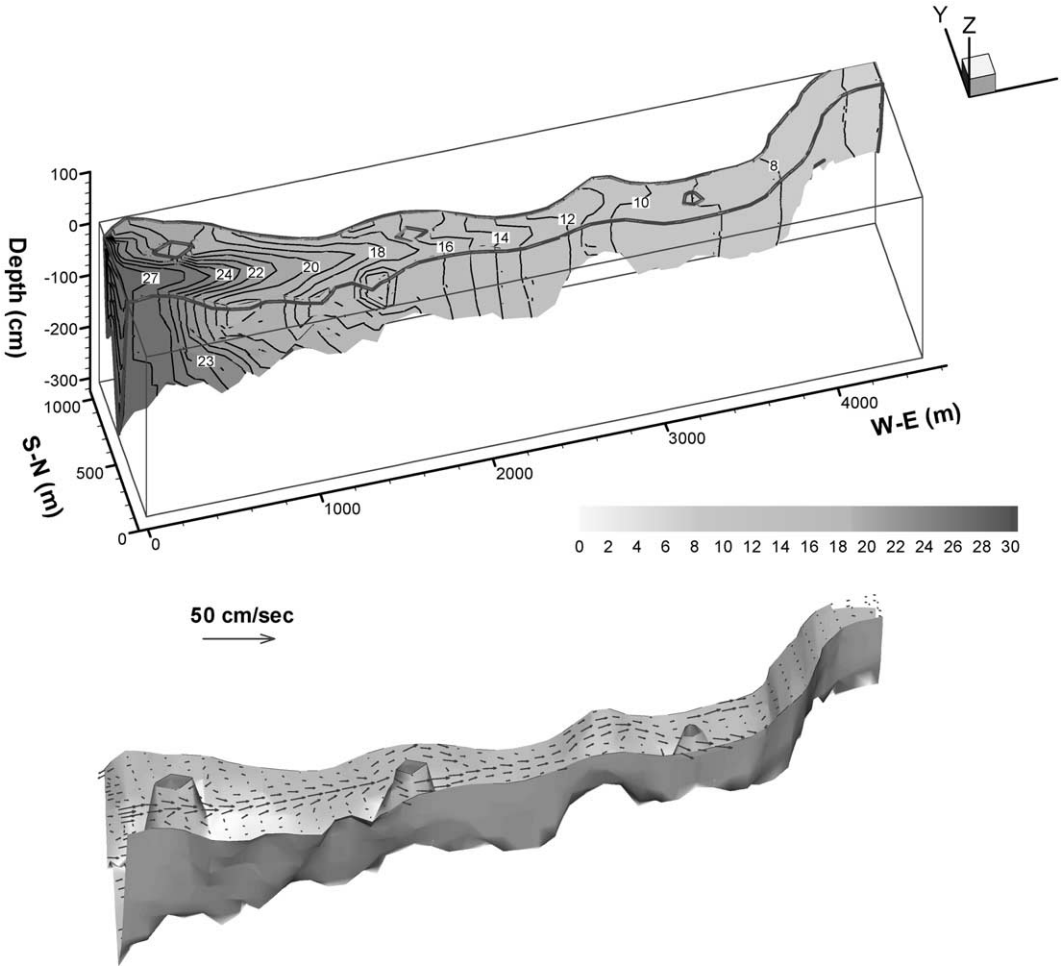

Fig. 9. Simulated velocity and salinity distributions in the Lower Alafia River at time = 7548.0 h when the water level is low during the flood tide.

7. Conclusions

The FSC method presented here contains two steps in solving the governing equations for shallow water flows. In the first step, an intermediate velocity field is solved with the explicit discretization of the horizontal pressure gradient terms. An intermediate free surface is then obtained based on the intermediate velocity field. This intermediate free surface is corrected by solving a five-diagonal system for the free surface change ($\Delta\eta$) over the time step Δt in the second step, before the final velocity field is solved. Unlike the semi-implicit method in [6,8] or the implicit method in [24], the formation of the five-diagonal matrix does not involve any matrix calculations, and is thus much easier to accomplish.

Similar to the semi-implicit method of Casulli and Cheng [6], the FSC method presented here does not involve the mode-splitting technique used by many 3-D hydrodynamic models for free-surface flows. Therefore, it does not have any consistency and synchronization problems associated with the mode-splitting technique. It is unconditionally stable with respect to gravitational waves, wind and bottom stresses, and vertical eddy viscosity terms.

The FSC method has been validated with various idealized test cases, before it was tested using field data collected in an estuary in Southwest Florida. Model simulations show that the FSC method works well for 3-D free-surface flows. Because of the simplicity of the method and the allowance of a larger simulation time step, the FSC method is an efficient method for modeling hydrodynamics of free-surface flows. When $\theta = 0$, there is no need to carry out the second step of the FSC method. In this case, the model uses the newest velocity field to calculate the fluxes in the vertically integrated continuity equation, resulting in an explicit 3-D model similar to that in [25]. Conversely, the FSC presented here can be easily added to existing numerical models that treat gravity waves explicitly.

References

[1] T.J. Simons, Verification of numerical models of Lake Ontario, Part 1. Circulation in spring and early summer, J. Phys. Ocean. 4 (1974) 507–523.

[2] R.V. Madala, S.A. Piacsek, A semi-implicit numerical model for baroclinic oceans, J. Comput. Phys. 23 (2) (1977) 167–178.

[3] Y.P. Sheng, A three-dimensional mathematical model of coastal, estuarine and lake currents using boundary fitted grid, Report No. 585, A.R.A.P. Group of Titan Systems, New Jersey, Princeton, NJ, 1986.

[4] A.F. Blumberg, G.L. Mellor, A description of a three-dimensional coastal ocean circulation model, Three Dimensional Coastal Ocean Models, American Geophysical Union, 1987, pp. 1–16.

[5] J.M. Hamrick, A three-dimensional environmental fluid dynamic computer code: theoretical and computational aspects, Special Report in Applied Marine Science and Ocean Engineering No 317, Virginia Institute of Marine Science, College of Willian & Mary, Gloucester Point, Virginia, 1992.

[6] V. Casulli, R.T. Cheng, Semi-implicit finite difference methods for three-dimensional shallow water flow, Int. J. Numer. Methods Fluids 15 (6) (1992) 629–648.

[7] V. Casulli, Semi-implicit finite difference methods for the two-dimensional shallow water equations, J. Comput. Phys. 86 (1) (1990) 56–74.

[8] V. Casulli, G.S. Stelling, Numerical simulation of 3D quasi-hydrostatic free-surface flows, J. Hydr. Eng. 124 (7) (1998) 678–686.

[9] V. Casulli, A semi-implicit finite difference methods for non-hydrostatic, free-surface flows, Int. J. Numer. Methods Fluids 30 (6) (1999) 425–440.

[10] X. Chen, Three-dimensional, hydrostatic and non-hydrostatic modeling of seiching in a rectangular basin, in: M.L. Spaulding, H.L. Butler (Eds.), Estuarine and Coastal Modeling, Proceedings of the 6th International Conference, ASCE, New York, 1999.

[11] G.H. Golub, C. van Loan, Matrix Computations, John Hopkins University Press, Baltimore, 1990.

[12] H.A. Van der Vorst, Bi-CGSTAB: a fast and smoothly converging variant of Bi-CG for solution of non-symmetric linear systems, SIAM J. Sci. Stat. Comput. 13 (1992) 631.

[13] X. Chen, Effects of hydrodynamics and sediment transport processes on nutrient dynamics in shallow lakes and estuaries, Ph.D. Dissertation, University of Florida, Gainesville, 1994.

[14] Y.P. Sheng, C. Villaret, Modeling the effect of suspended sediment stratification on bottom exchange process, J. Geophys. Res. 94 (1989) 14429–14444.

[15] M.B. Abbott, D.R. Basco, Computational Fluid Dynamics: An Introduction for Engineers, Wiley, New York, 1989.

[16] V. Casulli, E. Cattani, Stability, accuracy and efficiency of a semi-implicit method for three-dimensional shallow water flow, Comput. Math. Appl. 27 (4) (1994) 99–112.

[17] B.P. Leonard, A stable and accurate convective modeling procedure based on quadratic upstream interpolation, Comput. Methods Appl. Mech. Eng. 19 (1979) 59–98.

[18] P.L. Roe, Some contributions to the modeling of discontinuous flows, Lect. Appl. Math. 22 (1985) 163–193.

[19] R.W. Griffiths, P.F. Linden, The stability of vortices in a rotating, stratified fluid, J. Fluid Mech. 105 (1981) 283–316.

[20] I.D. James, Advective schemes for shelf sea models, J. Mar. Syst. 8 (1996) 237–254.

[21] B. Tartinville, E.P. Deleersnijder Lazure, R. Proctor, K.G. Ruddick, R.E. Uittenbogaard, A coastal ocean model intercomparison study for a three-dimensional idealized test case, Appl. Math. Modell. 22 (1998) 507–523.

[22] X. Chen, modeling hydrodynamics and salt transport in the Alafia River, Florida using a free-surface correction method, revised for Estuaries.

[23] X. Chen, A fully hydrodynamic model for three-dimensional, free-surface flows, Int. J. Numer. Methods Fluids, in press.

[24] M.M. Namin, B. Lin, R.A. Falconer, An implicit numerical algorithm for solving non-hydrostatic free-surface flow problems, Int. J. Numer. Methods Fluids 35 (2001) 341–356.

[25] J. Sündermann, Die hydrodynamisch-numerische Berechnung der Vertikalstruktur von Bewegungsvorgängen in Kanälen und Becken, Mitteilungen des Institut für Meeresfunde der Universität Hamburg, XIX, 1971, 104 pp.
[26] UNESCO. Algorithms for computation of fundamental properties of seawater, UNESCO Technical Papers in Marine Science, No. 44, UNESCO, Paris, 1983, 53 pp.